Increasing the interlayer spacing and generating closed pores to produce petroleum coke-based carbon materials for sodium ion storage

ZHUANG Hong-kun, LI Wen-cui, HE Bin, LV Jia-he, WANG Jing-song, SHEN Ming-yuan, LU An-hui*

(*State Key Laboratory of Fine Chemicals*, *School of Chemical Engineering*, *Dalian University of Technology*, *Dalian* 116024, *China*)

Abstract: Petroleum coke (PC) is a valuable precursor for sodium-ion battery (SIB) anodes due to its high carbon content and low cost. The regulation of the microcrystalline state and pore structure of the easily-graphitized PC-based carbon is crucial for creating abundant Na^+ storage sites. Here we used a precursor transformation strategy to increase the carbon interlayer spacing and generate abundant closed pores in PC-based carbon, significantly increasing its Na^+ storage capacity in the plateau region. This was achieved by introducing a large number of oxygen functional groups through mixed acid treatment and then using high-temperature carbonization to decompose the oxygen functional groups and rearrange the carbon microcrystallites, resulting in a transition from open to closed pores. The optimized samples provide a large reversible capacity of 356.0 mAh g^{-1} at 0.02 A g^{-1}, of which approximately 93% is below 1.0 V. Galvanostatic intermittent titration (GITT) and in-situ X-ray diffraction (XRD) analysis indicate that the sodium storage capacity in the low voltage plateau region involves a joint contribution of interlayer insertion and closed pore filling processes. This study presents a comprehensive method for the development of high-performance carbon anodes using low-cost and highly aromatic precursors.

Key words: Sodium ion battery; Petroleum coke; Carbon anode; Closed pore; Sodium ion storage

1 Introduction

The production of petroleum coke (PC), a by-product of oil refining, has been steadily increasing in tandem with advancements in crude oil refining technology[1–5]. However, the PC, especially with high sulfur content ($S \geqslant 3\%$), is directly burned as fuel in the cement industry and power plants, which lead to low-level utilization of PC and environmentally unfriendly[6–9]. Therefore, the investigation of novel sustainable pathways facilitating the value-added utilization of PC is imperative.

Several methods have been employed to transform PC into high value-added materials, such as carbon electrode materials, taking the advantages of its high carbon content, low ash content and volatile, and low economic cost[1,10–12]. Moreover, the heteroatoms, such as S in the PC can be removed after calcination at high temperatures, which optimizes the electronic structure of the carbon electrode materials[13–15]. Fan et al. prepared artificial graphite as anode materials for Li-ion batteries from PC by carbonization at 2400–3000 °C[16]. Similarly, Qiu et al. successfully synthesized porous carbon cathode materials by a KOH activation for Li-ion capacitor, which shows a high energy density (231 Wh kg^{-1}) and ultralong cycling life[17]. These results indicate that PC is a promising precursor for preparing carbon electrodes material. However, high temperature treatment requires high energy consumption and the KOH activation process causes corrosion of the facilities. Thus, the imperative objective is to research and develop cutting-edge carbon electrode materials for batteries in an efficient and environmentally friendly way.

Carbon materials have attracted considerable attention as anodes for alkali metal-ion batteries, such as sodium-ion batteries (SIBs), lithium-ion batteries (LIBs), and potassium-ion batteries (PIBs), because of their low-cost, nontoxicity, and controllable structures[18,19]. SIBs are promising rechargeable bat-

Received date: 2024-03-14; **Revised date:** 2024-04-28

Corresponding author: LU An-hui, Professor. E-mail: anhuilu@dlut.edu.cn

Author introduction: ZHUANG Hong-kun, Master student. E-mail: hongkun@mail.dlut.edu.cn

Supplementary data associated with this article can be found in the online version.

teries for large-scale electrical energy storage due to the natural abundance and low cost of sodium resources[20–24]. Alcántara et al. reported the use of PC as raw materials to prepare carbon electrode materials at temperatures below 1 000 °C for SIBs with a discharge capacity of about 100 mAh g^{-1}, which is much low for practical application[8]. As one kind of soft carbon, PC is easily converted to graphitic carbon with narrow layer spacing during the carbonization, which is detrimental to sodium storage[25–27]. Thus, it is necessary to enhance Na^+ storage capacity for PC-based carbon.

In this work, we demonstrate a facile strategy to synthesize carbon electrode from PC with high Na^+ storage capacities by increasing the spacing of carbon layers and fabricating abundant closed pores in the PC-based carbon. Firstly, a mixed acid treatment is employed to introduce oxygen functional groups into the PC and damage carbon microcrystals, resulting in disordered carbon structures. Subsequently, the pretreated PC is carbonized to decompose the oxygen functional groups and form open pores between 200-800 °C. The pre-formed open pores are transmuted into closed pores due to the carbon rearrangement at elevated temperatures (1 000 °C). Remarkably, the closed nanopores and expanded carbon interlayer spacing enable the PC-based carbon anode with excellent reversible capacity (356.0 mA h g^{-1} at 0.02 A g^{-1}) and high rate performance (186.3 mA h g^{-1} at 0.2 A g^{-1}) and good cycling stability (99.5% capacity retention after 100 cycles at 0.2 A g^{-1}). Additionally, the reversible specific capacity in the low-voltage plateau region (< 0.1 V) is about 93%, which improves the energy density of full SIBs. More importantly, the mechanism of sodium ion storage is investigated by kinetic analysis, galvanostatic intermittent titration technique (GITT) and in situ X-ray diffraction (XRD) , which indicates that the sodium storage capacity in the platform region is related to intercalation reaction and closed pore filling. This work might provide a general strategy for the fabrication of high-performance carbon anode materials for practical sodium-ion batteries from low-cost soft carbon precursors.

2 Experimental

2.1 Material synthesis

All reagents were obtained from commercial sources and used without further purification. Petroleum coke was oxidized with a mixture of concentrated sulfuric acid and concentrated nitric acid in a mass ratio of 7∶3 at 80 °C for 3 h. The pre-oxidized petroleum coke was subsequently washed with deionized water to neutral. The brown powder obtained after drying was named POPC. The POPC was subsequently carbonized in a tube furnace under argon flow for 2 h at temperatures of 1 000 °C, 1 200 °C, 1 400 °C and 1 600 °C at a heating rate of 4 °C min^{-1}, respectively. The amorphous carbon materials obtained after carbonization were denoted as POPC-x. where “x” represented the temperature of carbonization.

2.2 Material characterization

X-ray diffraction (XRD) patterns were measured with a Panalytical X’pert Pro Super X-ray diffractometer using Cu *K*a radiation (40 kV, 40 mA, λ = 0.154 18 nm) in a 2θ range of 10°–90°. The Fourier transform infrared (FT-IR) spectroscopy were measured on a Nicolet 6700 FT-IR spectrometer. X-ray photoelectron spectroscopy (XPS) was performed on an ESCALAB XI+ instrument to determine chemical bonding information. The morphologies of carbon materials were obtained from transmission electron microscopy (TEM, JEM-F200) instrument. The Raman spectra were characterized by an InVia Qontor Raman spectrometer with a diode laser excitation of 532 nm. Nitrogen adsorption isotherms were measured with an ASAP 2020 nitrogen adsorption-desorption analyzer (Micromeritics), and pore size distributions (PSDs) were calculated from the adsorption branches using nonlinear density functional theory (NL-DFT). Thermogravimetric analysis (TGA) was tested on a TG-DTA8122 instrument from room temperature to 1 000 °C at 10 °C min^{-1} under a nitrogen atmosphere. Carbon dioxide sorption isotherms were measured with an Autosorb-iQMP automated gas sorption analyzer (Quantachrome).

2.3 Electrochemical measurements

All electrochemical tests were performed in a coin cell (CR2032). A homogeneous slurry was formed by mixing the active material, conductive agent (CNT), and sodium alginate binder in deionized water at a weight ratio of 8∶1∶1. The slurry was coated on Cu foil and then dried under vacuum at 100 ℃ for 12 h to prepare the working electrode. The average loading mass of active materials was ~1.5 mg cm^{-2}. The electrolyte was 1 mol L^{-1} $NaClO_4$ in ethylene carbonate (EC) and diethyl carbonate (DEC) (1∶1 by volume). Sodium foil was used as counter electrode and glass fiber was used as membrane. All operations were performed in an argon-filled glove box. Discharge and charge tests were performed on a Land BT2000 battery test system (Wuhan, China) with a voltage range of 0.01–3 V.

3 Results and discussion

The XRD pattern (Fig. 1a) of PC exhibits a narrow and sharp peak at 25.5°, corresponding to the (002) crystal plane of graphitic sheets, indicating a high degree of graphitization[28]. In contrast, the (002) peak of POPC is centered at around 22.3° and is very broad, indicating an amorphous nature. The interlayer distances of PC and POPC are 0.349 and 0.398 nm, respectively, which are calculated using Bragg's law based on (002) peak[29]. These results indicate that the oxidation treatment decreases the degree of graphitization and crystallinity. As presented in Fig. 1b, the FT-IR of PC shows the stretching vibration peak of C=C (1 610 cm^{-1}) and the bending vibration (735 cm^{-1}) and symmetric stretching (1 380 cm^{-1}) of $-CH_3$[24,30]. POPC exhibits well-defined characteristic peaks of O−S−O (1 052 cm^{-1}), C−O−C (1 240 cm^{-1}), O=N−O (1340–1530 cm^{-1}) and C=O (1 720 cm^{-1}), while the peak of C=C became weaker and the peaks of $-CH_3$ disappeared. The results of FT-IR spectroscopy demonstrate that oxidation, nitration and sulfonation reactions occurred at the side chains, heterocycles and edges of petroleum coke molecules. The adsorption-desorption isotherms of PC and POPC in Fig. S1 exhibit typical Type I isotherms, confirming the microporous structures. The specific surface areas of PC and POPC are 1.20 and 3.98 $m^2 g^{-1}$,

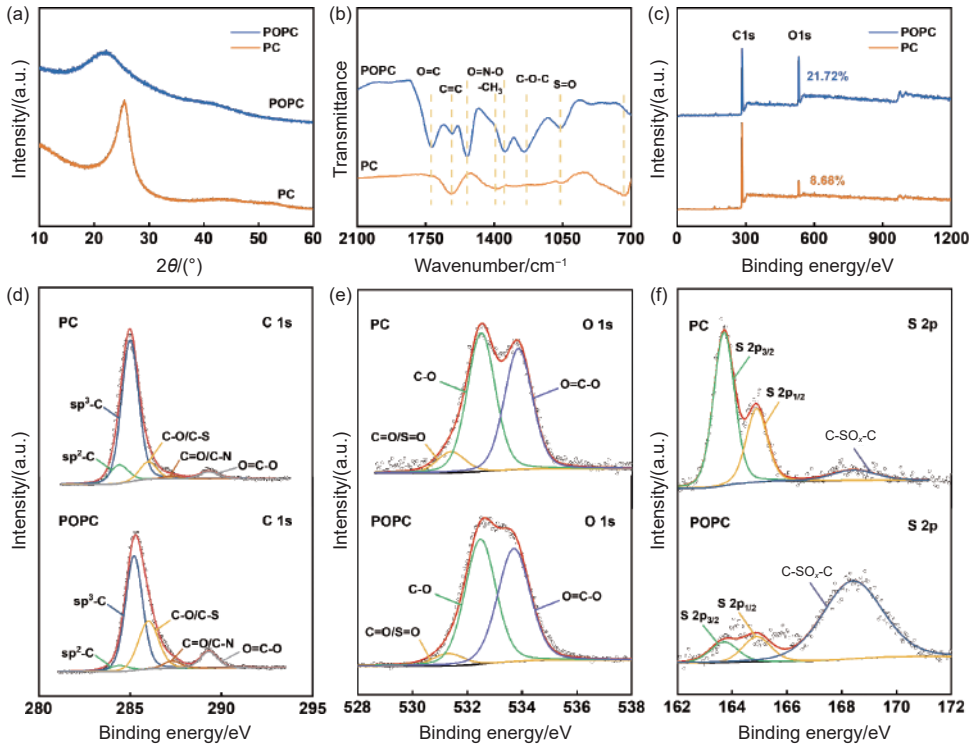

Fig. 1　(a) XRD patterns, (b) FT-IR spectra, (c) XPS spectra of PC and POPC. Deconvoluted high resolution (d) C 1s, (e) O 1s, and (f) S 2p spectra of PC and POPC

which indicates that the acid treatment step did not create pores on the surface of the petroleum coke. XPS was used to further characterize the surface chemical composition of PC and POPC. Both PC and POPC contain C, N, O and S elements (Table S1). As shown in Fig. 1c, the oxygen content of POPC is much higher than that of PC, proving that the oxidation process has grafted many oxygen functional groups on the surface of PC. The high-resolution XPS spectra of C 1s (Fig. 1d) can be deconvoluted into 6 peaks at 284.5, 285.4, 286.3, 287.4, 288.9 and 290 eV, respectively, which are attributed to sp^2—C, sp^3—C, C—O/C—S, C=O/C—N, O=C—O and π-π* transition (settled transition of aromatic carbon)[31–33]. It can be seen that the sp^2—C content of POPC decreased compared to PC, confirming the destruction of petroleum coke graphite microcrystalline structure by oxidation treatment. The distinct chemical states of O were additionally recognized in the O 1s spectrum (Fig. 1e), where the peaks centers at 531.4, 532.2 and 533.4 eV can be attributed to C=O/S=O, C—O and O—C=O, respectively[34]. Moreover, the peaks at 163.7 and 164.9 eV in the S spectrum (Fig. 1f) can be assigned to the S $2p_{3/2}$ and S $2p_{1/2}$ peaks of C—S—C covalent bond, while the peak at 168.4 eV corresponds to C—SO_x—C group. It appears that the percentage of C—SO_x—C in POPC increase significantly. The XPS and FT-IR results reveal that the mixed acid treatment successfully increases the oxygen content of the material by introducing a large number of oxygen functional groups and can make the material more disordered. In addition, these oxygen functional groups can impede the migration and growth of carbon microcrystals, hindering the long-range development of carbon microstructures and successfully converting petroleum coke from a soft carbon precursor to a hard carbon precursor. More importantly, these oxygen functional groups decompose during subsequent high-temperature treatment, causing the material to form a porous structure. The limited mobility of the carbon layer may result in the formation of a significant number of closed nanopores in POPC following carbon rearrangement at high temperatures, which is beneficial to the storage of Na^+ in the low-voltage plateau region.

Next, we carbonized POPC under argon flow at different temperatures to obtain the anode material for sodium-ion battery, and also carbonized PC at 1 400 °C for comparison. Obviously, as shown in Fig. 2a-b, there is a clear difference in the structure of PC and POPC after carbonization. PC-1400 exhibits a highly graphitized structure, which can be seen in the

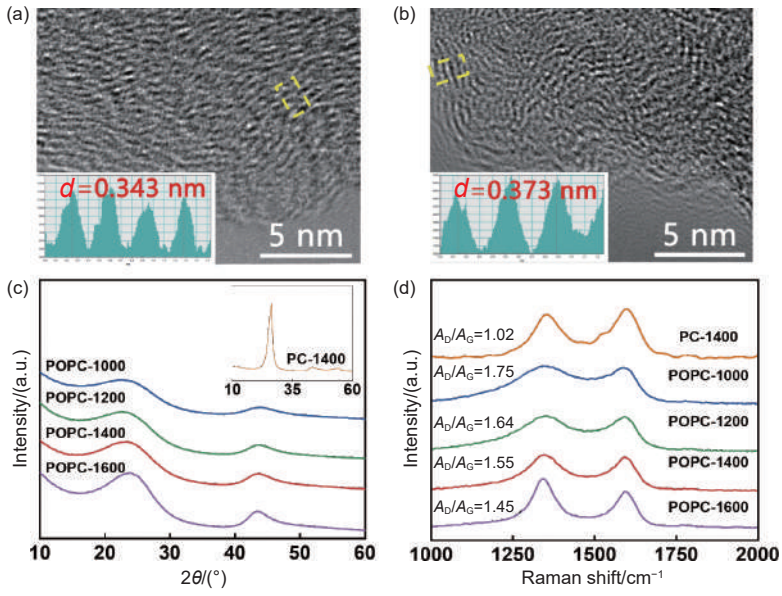

Fig. 2 TEM images of (a) PC-1400 and (b) POPC-1400. (c) XRD patterns, and (d) Raman spectra of POPC-1000, POPC-1200, POPC-1400, POPC-1600 and PC-1400

apparent long-range ordered parallel carbon layers. On the contrary, the graphite layer of POPC-1400 bends and exhibits a disordered structure throughout the entire region. Furthermore, atomic migration causes interplay and folding of the graphite layers, resulting in the formation of numerous closed pores.

The XRD patterns (Fig. 2c) show broad diffraction peaks at ~24° and ~43°, which is related to the (002) and (100) diffraction of graphite-like domains in disordered carbons, respectively. As the carbonization temperature increases, the (002) peaks gradually move to a higher angle, corresponding to a decrease in the interlayer spacing. The interlayer distance of POPC-1400 is calculated to be 0.373 nm, which is in agreement with the value observed from the HRTEM images. The average width (L_a) and average thickness (L_c) of graphite-like microcrystals were calculated based on the Debye-Scherrer equation[33]. The L_a and L_c of POPC samples increased with the increase of the carbonization temperature. And the empirical parameter R was used to measure the ordering degree of HC [35]. As the temperature increasing from 1 000 to 1 600 °C, the R value of POPC increase from 1.62 to 2.09, which means that the material became more ordered at higher temperatures. However, the XRD pattern of PC-1400 shows a sharp diffraction peak at 26.2° and the average size of graphite microcrystals was larger than that of all POPC-x samples, indicating a significantly higher degree of crystallinity compared to POPC-x. The interlayer spacing of PC-1400 is calculated to be 0.340 nm, which is close to the HRTEM results. Table 1 provides a summary of the structural parameters of these materials. It can be seen that POPC shows larger d_{002} values and smaller L_c and L_a values compared to PC at the same carbonization temperature, which indicates that pre-oxidation can effectively retard the development of microcrystalline structures during carbonization. Raman spectra were performed on all samples to estimate the defects in the carbon material. As shown in Fig. 2d, two obvious main peaks located at 1 350 and 1 595 cm^{-1} correspond to disordered D band and graphite G band, respectively. The integral intensity ratio (A_D/A_G) is commonly used to assess the disorder of carbon materials. The fitted results (Fig. S2) show a gradual decrease in the value of A_D/A_G of POPC with increasing carbonization temperature, indicating an enhanced ordered structure in the material. The XRD and Raman results are in agreement, verifying the augmented ordering of POPC-x as the carbonization temperature increases.

The N_2 sorption measurement results in Fig. S3 show that all samples exhibited a typical type I isotherm, indicating the microporous structures in POPC-x samples. POPC-1000 exhibits a specific surface area of 532.6 $m^2\ g^{-1}$ and a pore volume of 0.21 $cm^{-3}\ g^{-1}$. In contrast, POPC-1200 shows a much lower specific surface area of 12.7 $m^2\ g^{-2}$ and a pore volume of 0.02 $cm^{-3}\ g^{-1}$, indicating that the pore structure of the obtained samples could be effectively adjusted during the carbonation process. The specific surface area of the materials gradually decreased with increasing temperature, and POPC-1400 and POPC-1600 showed a negligible amount of N_2 adsorption. In addition, PC-1400 also exhibits a very low specific surface area.

In order to clarify the origin and evolution of microporosity in the material during carbonization, TGA of PC and POPC was performed at room temperature to 1 000 °C at 10 °C min^{-1} under N_2 flow. The TGA curve (Fig. 3a) shows that PC has only about 10% weight loss from room temperature to 1 000 °C, which could be attributed to the decomposition of small amounts of oxygen functional groups and processes such as molecular volatilization and hydrocarbon skeleton cleavage. The differential thermogravi-

Table 1　Structural parameters of POPC-1000, POPC-1200, POPC-1400, POPC-1600 and PC-1400

Samples	d_{002}/nm	L_a/nm	L_c/nm	R value	True density/(g cm^{-3})	Closed pore Volume/($cm^3\ g^{-1}$)
PC-1400	0.340	3.94	5.26	5.67	2.22	–
POPC-1000	0.383	1.00	3.14	1.62	2.13	0.03
POPC-1200	0.382	1.03	3.41	1.67	1.98	0.06
POPC-1400	0.373	1.04	3.69	1.85	1.89	0.08
POPC-1600	0.369	1.14	3.97	2.09	1.78	0.11

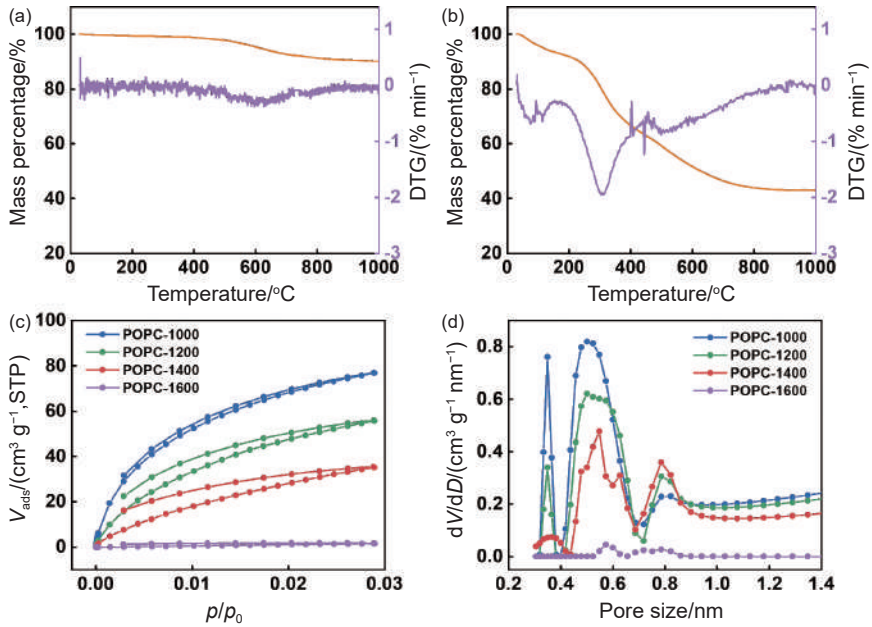

Fig. 3 TG-DTG curves of (a) PC and (b) POPC. (c) CO_2 sorption isotherms and (d) pore size distributions of POPC-1000, POPC-1200, POPC-1400 and POPC-1600

metric (DTG) curves of PC are also relatively flat, indicating that there were no violent decomposition reactions that could lead to mass loss during the warming process. In contrast, the TGA curve of POPC (Fig. 3b) is very steep, with a loss of 58% mass during heating. The DTG curve shows a rapid decomposition of POPC around 300 °C, which is usually associated with the decomposition of hydroxyl, carboxyl and ester functional groups. The XPS analysis results for POPC-x are presented in Table S2, which show that the total content of nitrogen, oxygen, and sulfur elements decreased gradually with the increase of carbonization temperature. The oxygen content of POPC was 21.72%, which decreased to 4.94% upon increasing the temperature to 1 000 °C. The observed decrease in oxygen content is consistent with the TGA results, indicating that the oxygen functional groups decompose during the temperature increase, resulting in the loss of mass of the material. The decomposition of the oxygen functional group leads to the loss of carbon atoms and the formation of various defects in the material, which is the source of the pores in the material.

Considering that CO_2 is more accessible to the ultra-micropores (pore diameter < 1 nm) in the sample at 0 °C, CO_2 adsorption tests were performed on POPC-x to analyze the alterations in microporous structures under varying carbonization temperatures. It is obvious from Fig. 3c that the CO_2 adsorption of POPC decreases significantly with increasing temperature, and there is almost no CO_2 adsorption when the temperature rises to 1 600 °C. The DFT pore size distribution (Fig. 3d) showed that the ultra-micropores of all POPC samples were concentrated in the pore size range of 0.3 to 0.8 nm. However, the ultra-microporous volume decreased from 0.226 $cm^3\ g^{-1}$ for POPC-1000 to 0.004 $cm^3\ g^{-1}$ for POPC-1600, which implies that some ultra-microporous pores were transformed into closed nanopores during the high temperature carbonization.

It's important to note that the gas adsorption method can solely detect open pores that are accessible to the gas. However, many closed internal pores are still present in most carbon materials. To further quantify the closed nanopore structure in the material, a true density analysis was performed using the He replacement method. Because of the extremely minute aerodynamic diameter of He molecules, which can permeate nearly all open pores except closed ones, the true density test provides an accurate value of the skeletal density of the tested samples[23]. Graphite is considered to be a perfectly layered carbon material

without closed pores, with a true density of 2.26 g cm^{-3}. Therefore, the closed pore volume of porous carbon can be calculated as follows:

$$V_{\text{closed pores}} = 1/\rho_{\text{ture}} - 1/2.26 \quad (1)$$

The structural characteristics of the materials are outlined in Table 1. It is obvious that the skeleton density of POPC-x decreases with the increase of carbonization temperature. Combining the results of gas adsorption/desorption and true density tests, the open pore volume of POPC-x keeps decreasing with increasing temperature, while the closed pore volume keeps increasing, indicating that the open pores tend to close during the carbonization at high temperature. The POPC-x carbonized at higher temperatures have larger sodium cluster in the pore filling space. Furthermore, the true density of PC-1400 is similar to that of graphite with almost no closed pores, suggesting that a significant quantity of closed pores stems from nanopores formed through the decomposition of oxygen functional groups. In brief, by means of pre-oxidation followed by high-temperature carbonization, the interlayer spacing of PC has been successfully expanded, concomitantly generating closed pores within its carbonaceous framework, thus serving to enhance its sodium storage capability.

Thus, the above-mentioned physicochemical characteristics suggest that the altered carbonization process of POPC successfully results in the generation of a substantial of closed pores in the resulting carbon, which would alter the storage behavior of sodium ions. Next the electrochemical properties of the obtained samples were evaluated in a half-cell configuration using sodium metal as counter electrode. The Fig. 4a displays the initial galvanostatic charge-discharge (GCD) curves for POPC-1000, POPC-1400, and PC-1400 anodes at a constant current density of

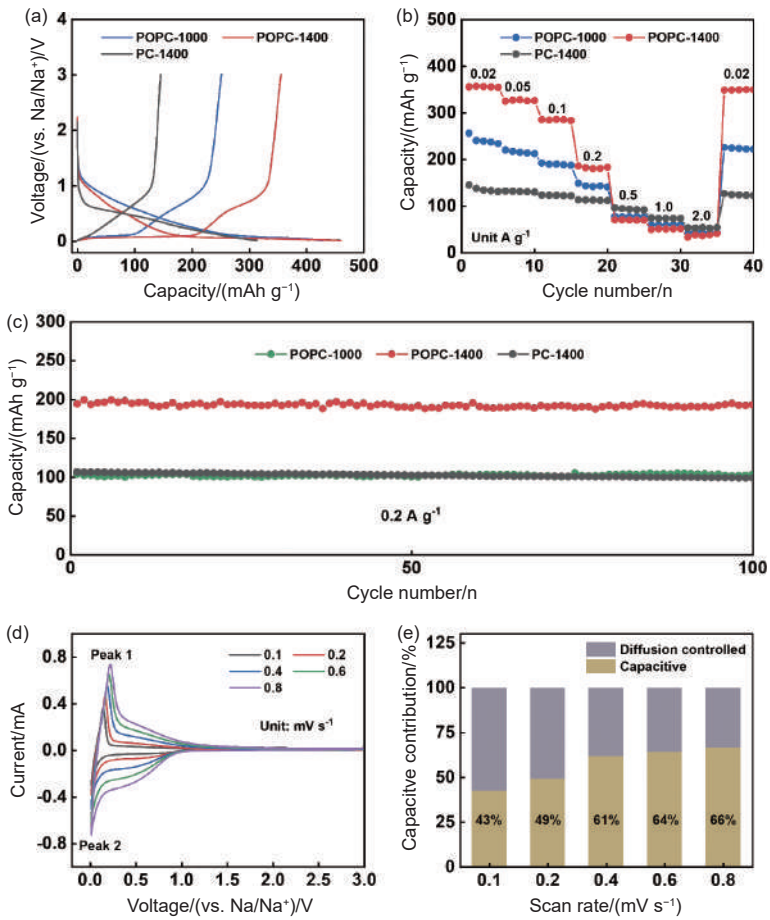

Fig. 4　(a) GCD curves in the 1st cycle at a current density of 0.02 A g^{-1}, (b) rate performance, and (c) long-term cycling stability of POPC-1000, POPC-1400, and PC-1400 anodes. (d) CV curves at various scan rates, (e) contribution ratios of capacitive process and diffusion-controlled at various scan rates of POPC-1400 anode

0.02 A g^{-1}. Due to a narrow interlayer spacing and absence of closed pores, PC-1400 did not exhibit a plateau region at low voltage, resulting in a reversible specific capacity of only 145.4 mAh g^{-1}. POPC-1000 and POPC-1400 anodes show 2 distinctly different potential regions: the plateau region below 0.1 V and the slope region above 0.1 V. The initial charging capacity of POPC-1000 is 251.5 mAh g^{-1}, the initial coulombic efficiency (ICE) is only 58.7%, and the specific capacity in the plateau region is 75.2 mAh g^{-1}. When the carbonization temperature is raised to 1 400 °C, the initial charging capacity was 356.0 mAh g^{-1}, the ICE increased to 77.3%, and the specific capacity in the plateau region increased to 199.6 mAh g^{-1}. Fig. S5 shows the comparison of the electrochemical properties in this work with those of the reported sodium-ion battery materials. The significant improvement in ICE upon temperature increase demonstrated a reduction in irreversible sodium ion storage behavior in the first cycle, which may be related to the reduction in the specific surface area available for solid electrolyte interphase (SEI) formation. In addition, the open to closed pore transition leads to an increase in the closed pores in the material, increasing the specific capacity of the plateau region. The rate performance in the current density range of 0.02–2 A g^{-1} is further given in Fig. 4b. The cycling performance of all samples at 0.2 A g^{-1} current density is shown in Fig. 4c, where POPC-1400 shows a high capacity retention of 99.5% after 100 cycles. POPC-1000 anode showed a capacity of 251.5 mAh g^{-1} during the first cycle, however, the capacity was only 226.1 mAh g^{-1} after the rate capability test, indicating that the sample has a relative weak ability to resist high-current charging and discharging. The cycling performance was tested after rate performance, thus POPC-1000 and PC-1400 exhibits the similar capacity. Fig. S6 illustrates the long-term cycling performance of POPC-1000, POPC-1400 and PC-1400 at 0.5 A g^{-1}. Notably, after 500 cycles, POPC-1400 exhibited a capacity retention rate of over 99%, showcasing exceptional cycling stability. Fig. S7 shows the electrochemical performance of both POPC-1200 and POPC-1600. Meanwhile, POPC-1200 exhibited intermediate performance between POPC-1000 and POPC-1400. As for POPC-1600, the further reduction of micropores led to a decline in the specific capacity of the slope region, resulting in no further increase in its reversible specific capacity. Fig. S8 illustrates the relationship between the carbonization temperature of POPC-x and the composition of their reversible capacity. It can be seen that changing the carbonation temperature increases the Na^+ storage capacity of POPC-x by increasing the specific capacity of the plateau region.

The reaction kinetics were investigated by cyclic voltammetry (CV) measurements to better understand the storage behavior of Na^+ in POPC-1400. As shown in Fig. 4d, POPC-1400 shows a retained shape and well-defined peaks over a range of scan rates from 0.1 to 0.8 mV s^{-1}, indicating the small polarization and high stability of the fabricated electrode. Scanning to around 0.1 V, a pair of oxidation/reduction peaks appear, which are attributed to the reversible sodium storage reaction of the hard carbon and correspond to the plateau region. The weak peaks in the wide potential range of 0.2–1 V correspond to the slope region. Indeed, the area of the CV loop indicates the combined energy storage of pseudo-capacitive behavior and diffusion-controlled processes[26]. The respective energy storage mechanism can be investigated by analyzing the log-linear relationship between the peak current (i) and the scan rate (v), as described as follows:

$$\log(i) = \log(a) + b\log(v) \tag{2}$$

where a, b are adjustable parameters. b values are well defined: b = 0.5 for diffusion-controlled processes and b = 1.0 for pseudo-capacitive behavior. According to Fig. S9a-b, the b values for the anode and cathode peaks are close to 0.5, indicating that pseudo-capacitive behavior dominates the POPC-1400 electrode. Specifically, the contribution of pseudocapacitance to sodium storage at different scan rates can be quantitatively assessed according to Equation (3):

$$i = k_1 v + k_2 v^{1/2} \tag{3}$$

where $k_1 v$ and $k_2 v^{1/2}$ denote the contribution of pseudo-

capacitance behavior and diffusion control processes, respectively. The results of the calculation are shown in Fig. 4e. As the scan rate increases from 0.1 to 0.8 mV s^{-1}, the contribution of the capacitive process increases from 43% to 66%, indicating that the POPC-1400 anode has good kinetic behavior even at high rates.

Further comprehension of the storage mechanism of Na^+ in hard carbon, galvanostatic intermittent titration technique (GITT) measurements were performed on both POPC-1400 and PC-1400 anodes at a pulsed current of 0.02 A g^{-1} to evaluate the apparent diffusion coefficient (D_{Na^+}) of Na^+ during charging and discharging. The diffusion coefficient was determined according to Equation (4):

$$D = \frac{4}{\pi\tau}\left(\frac{m_B V_m}{M_B S}\right)^2\left(\frac{\Delta E_S}{\Delta E_\tau}\right)^2 \quad (4)$$

where τ (s), m_B (g), V_M (cm^3 mol^{-1}), M_B (g mol^{-1}) and S (cm^2) represent the pulse duration, the active mass of the electrode, the molar volume, the molecular weight and the active surface area of the electrode, respectively. And ΔE_S and ΔE_τ are derived from the GITT curves. The apparent diffusion coefficient (D_{Na^+}) curves during the discharge-charge process are shown in Fig. 5a-b. During the discharge process of the POPC-1400 anode, the adsorption sites on the electrode surface decreased and the D_{Na^+} continued to decrease. At discharge to 0.1 V, D_{Na^+} increases, indicating a change in the sodium storage process. In the low voltage plateau region, D_{Na^+} first decreases in the initial phase and then increases near the cut-off voltage. The abrupt decrease in D_{Na^+} at 0.05 V may be attributed to the sluggish kinetics of Na^+ insertion into the closed nanopores. Conversely, the subsequent rise near the cut-off voltage may result from the adsorption and aggregation of Na^+ within these closed nanopores. However, due to the absence of enclosed pores in PC-1400, its diffusion coefficient curve did not exhibit a reverse increase near the cutoff voltage.

The changes in the electrode structure of POPC-1400 during charging and discharging were further effectively monitored using time-resolved in-situ XRD (Fig. 5c). In the initial slope region, the (002) peak position is not shifted. With the discharge in the plateau region and being sodiated, the peak position shifts slightly to a lower angle, suggesting an expansion of the interlayer distance. Once the electrode starts the charging process, the (002) peak shift returns to a higher angle, indicating a shortening of the interlayer distance. More detailed graphical results are presented in Fig. S10, indicating the intercalation sodium storage behavior in the material. By combining the GITT and in-situ XRD results, the conclusion drawn is that the plateau capacity is primarily arises from in-

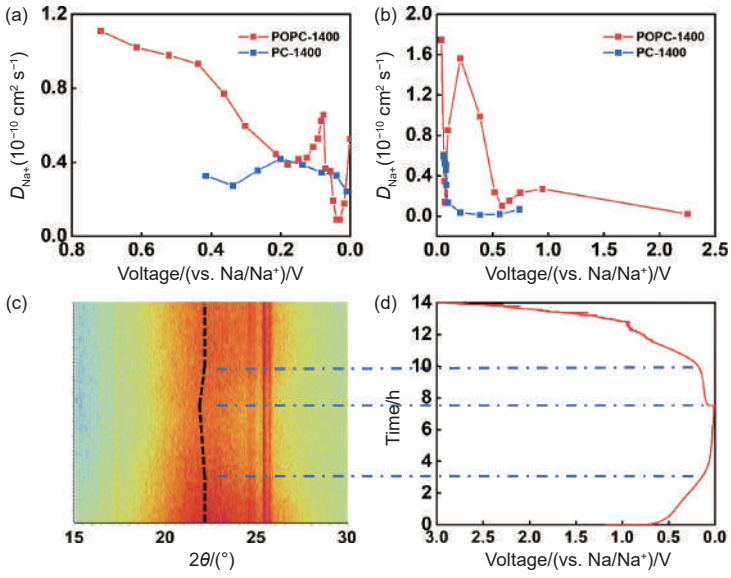

Fig. 5　Na^+ apparent diffusion coefficients calculated from the GITT potential profiles of POPC-1400 for (a) discharge process and (b) charge process during the second cycle. (c) In situ XRD mapping of POPC-1400 at various stages during the first charge-discharge process

terlayer intercalation and pore filling. Derived from the theoretical specific capacity of sodium metal (1 128 mAh cm^{-3}) and the closed pore volume, the maximum possible capacity resulting from full closed pore filling can be calculated[23]. The plateau capacity of the POPC-1400 electrode is 199.6 mAh g^{-1}, surpassing the maximum capacity calculated by fully filling the closed pore volume (96.6 mAh g^{-1}). Therefore, part of the platform capacity must originates from the intercalation contribution. This is also consistent with the "adsorption-intercalation-filling" mechanism reported in the literature[36–38]. Thanks to the high platform capacity, POPC-1400 exhibits a high reversible capacity.

4 Conclusion

In summary, we have developed a disordered hard carbon anode for SIBs based on a simple mixed acid treatment and high-temperature carbonization strategy. Using low-cost PC as the precursor, we disrupted the microcrystalline structure of PC through mixed acid treatment, expanded the carbon interlayer spacing, and introduced a significant quantity of oxygen functional groups. The oxygen functional groups were then decomposed at high temperature to form open pores, followed by a carbon rearrangement process that resulted in a transition from open to closed pores, thereby inducing a disordered carbon structure rich in closed pores. POPC-1400 has sufficient Na^+ diffusion layer spacing and a large number of closed pores, showing a high reversible capacity (356.0 mAh g^{-1} at 0.02 A g^{-1}) with an initial coulombic efficiency of 77.3%, which is much better than the long-range ordered pristine petroleum coke derived carbon. The mechanism of charge storage and sodium ion storage was also investigated, and it was proved by GITT and in-situ XRD to be consistent with the "adsorption-intercalation-filling" mechanism. This study not only reports a simple method to apply low-cost petroleum coke to SIBs, but also provides a reasonable design strategy for high-performance hard carbon materials.

Data availability statement

The data that support the findings of this study are openly available in Science Data Bank at https://cstr.cn/31253.11.sciencedb.j00125.00030 and https://doi.org/10.57760/sciencedb.j00125.00030.

Acknowledgements

This work was financially supported by the National Natural Science Foundation of China (Nos. 22075038, 22209019), the Fundamental Research Funds for the Central Universities (No. DUT22LAB607), and National Key Research and Development Project (2021YFA1500300).

References

[1] Hu H, Wu M. Heavy oil-derived carbon for energy storage applications[J]. Journal of Materials Chemistry A, 2020, 8(15): 7066-7082.

[2] Prajapati R, Kohli K, Maity S K. Slurry phase hydrocracking of heavy oil and residue to produce lighter fuels: An experimental review[J]. Fuel, 2021, 288: 119686.

[3] Apicella B, Russo C, Senneca O. Analytics for recovery and reuse of solid wastes from refineries[J]. Energies, 2022, 15(11): 4026.

[4] Zhu F, Song W L, Ge J B, et al. High-purity graphitic carbon for energy storage: Sustainable electrochemical conversion from petroleum coke[J]. Advanced Science, 2023.

[5] Agarwal P, Sharma D K. Studies on the desulfurization of petroleum coke by organorefining and other chemical and biochemical techniques under milder ambient pressure conditions[J]. Petroleum Science and Technology, 2011, 29(14): 1482-1493.

[6] Xiang D, Li P, Yuan X. Parameter optimization and exergy efficiency analysis of petroleum coke-to-hydrogen by chemical looping water splitting process with CO_2 capture and self-heating[J]. Fuel, 2022, 324: 124475.

[7] Reis T. Coke, desulfurize and calcine. Coke quality and its control[J]. Hydrocarbon Processing, 1975, 54(6): 97-104.

[8] Alcantara R, Mateos J M J, Tirado J L. Negative electrodes for lithium- and sodium-ion batteries obtained by heat-treatment of petroleum cokes below 1000 degrees C[J]. Journal of the Electrochemical Society, 2002, 149(2): A201-A205.

[9] Li P, Liu J Y, Wang Y W, et al. Synthesis of ultrathin hollow carbon shell from petroleum asphalt for high-performance anode material in lithium-ion batteries[J]. Chemical Engineering Journal, 2016, 286: 632-639.

[10] AlAreeqi S, Bahamon D, Polychronopoulou K, et al. Insights into the thermal stability and conversion of carbon-based materials by using ReaxFF reactive force field: Recent advances and future directions[J]. Carbon, 2022, 196: 840-866.

[11] Virla L D, Montes V, Wu J F, et al. Synthesis of porous carbon from petroleum coke using steam, potassium and sodium: Combining treatments to create mesoporosity[J]. Microporous and Mesoporous Materials, 2016, 234: 239-247.

[12] Li P, Hwang J Y, Park S M, et al. Superior lithium/potassium storage capability of nitrogen-rich porous carbon nanosheets derived from petroleum coke[J]. Journal of Materials Chemistry A, 2018, 6(26): 12551-12558.

[13] Li Q Y, Li Z S, Lin L, et al. Facile synthesis of activated carbon/carbon nanotubes compound for supercapacitor application[J]. Chemical Engineering Journal, 2010, 156(2): 500-504.

[14] Jaleh B, Nasrollahzadeh M, Eslamipanah M, et al. The role of carbon-based materials for fuel cells performance[J]. Carbon, 2022, 198: 301-352.

[15] Pan L, Wang Y X, Hu H, et al. 3D self-assembly synthesis of hierarchical porous carbon from petroleum asphalt for supercapacitors[J]. Carbon, 2018, 134: 345-353.

[16] Fan C L, He H, Zhang K H, et al. Structural developments of artificial graphite scraps in further graphitization and its relationships with discharge capacity[J]. Electrochimica Acta, 2012, 75: 311-315.

[17] Qiu Z J, Cui Y P, Wang D D, et al. Dual carbon Li-ion capacitor with high energy density and ultralong cycling life at a wide voltage window[J]. Science China-Materials, 2022, 65(9): 2373-2384.

[18] Chen Y X, Xi B J, Huang M, et al. Defect-selectivity and "order-in-disorder" engineering in carbon for durable and fast potassium storage[J]. Advanced Materials, 2022, 34: 2108621.

[19] Geng C, Chen Y X, Shi L L, et al. Design of active sites in carbon materials for electrochemical potassium storage[J]. New Carbon Materials, 2022, 37(3): 461-483.

[20] Nagmani, Pahari D, Verma P, et al. Are Na-ion batteries nearing the energy storage tipping point? - Current status of non-aqueous, aqueous, and solid-sate Na-ion battery technologies for sustainable energy storage[J]. Journal of Energy Storage, 2022, 56.

[21] Jafta C J. Grid scale energy storage: The alkali-ion battery systems of choice[J]. Current Opinion in Electrochemistry, 2022, 36: 101130.

[22] Xu Z, Wang J. Toward emerging sodium-based energy storage technologies: From performance to sustainability[J]. Advanced Energy Materials, 2022, 12(29): 2201692.

[23] Li Y, Lu Y, Meng Q, et al. Regulating pore structure of hierarchical porous waste cork-derived hard carbon anode for enhanced Na storage performance[J]. Advanced Energy Materials, 2019, 9(48): 1902852.

[24] Sun F, Wang H, Qu Z, et al. Carboxyl-dominant oxygen rich carbon for improved sodium ion storage: Synergistic enhancement of adsorption and intercalation mechanisms[J]. Advanced Energy Materials, 2021, 11(1): 2002981.

[25] Zuo J H, Liu Z Y, Jiang H N, et al. Sodium titanate nanowires for Na^+-based hybrid energy storage with high power density[J]. Susmat, 2022, 2(6): 720-730.

[26] Wang K, Sun F, Wang H, et al. Altering thermal transformation pathway to create closed pores in coal-derived hard carbon and boosting of Na^+ plateau storage for high-performance sodium-ion battery and sodium-ion capacitor[J]. Advanced Functional Materials, 2022, 32(34): 2203725.

[27] Cai C, Chen Y, Hu P, et al. Regulating the interlayer spacings of hard carbon nanofibers enables enhanced pore filling sodium storage[J]. Small, 2022, 18(6): 2105303.

[28] Zhang T, Li C, Wang F, et al. Recent advances in carbon anodes for sodium-ion batteries[J]. The Chemical Record, 2022, 22(10): e202200083.

[29] Chen X, Tian J, Li P, et al. An overall understanding of sodium storage behaviors in hard carbons by an "adsorption-intercalation/filling" hybrid mechanism[J]. Advanced Energy Materials, 2022, 12(24): 2200886.

[30] Lu Y, Zhao C, Qi X, et al. Pre-oxidation-tuned microstructures of carbon anodes derived from pitch for enhancing Na storage performance[J]. Advanced Energy Materials, 2018, 8(27): 1800108.

[31] Hu X D, Sun X H, Yoo S J, et al. Nitrogen-rich hierarchically porous carbon as a high-rate anode material with ultra-stable cyclability and high capacity for capacitive sodium-ion batteries[J]. Nano Energy, 2019, 56: 828-839.

[32] Yin B, Liang S, Yu D, et al. Increasing accessible subsurface to improving rate capability and cycling stability of sodium-ion batteries[J]. Advanced Materials, 2021, 33(37): 2100808.

[33] Zhao G, Yu D, Zhang H, et al. Sulphur-doped carbon nanosheets derived from biomass as high-performance anode materials for sodium-ion batteries[J]. Nano Energy, 2020, 67: 104219.

[34] Zhang MM, Yan D, Li WC. Regulation of dual-ion batteries via the defects design in carbon electrode based on the different storage behaviors of PF_6^- and Li^+[J]. Journal of Power Sources, 2022, 527: 231169.

[35] Stevens D A, Dahn J R. The mechanisms of lithium and sodium insertion in carbon materials[J]. Journal of the Electrochemical Society, 2001, 148(8): A803-A811.

[36] Morikawa Y, Nishimura SI, Hashimoto RI, et al. Mechanism of sodium storage in hard carbon: An X-ray scattering analysis[J]. Advanced Energy Materials, 2020, 10(3): 1903176.

[37] Cheng D, Zhou X, Hu H, et al. Electrochemical storage mechanism of sodium in carbon materials: A study from soft carbon to hard carbon[J]. Carbon, 2021, 182: 758-769.

[38] Jin Y, Sun S, Ou M, et al. High-performance hard carbon anode: Tunable local structures and sodium storage mechanism[J]. ACS Applied Energy Materials, 2018, 1(5): 2295-2305.